Crystallization of magnetic skyrmions in MnSi investigated by neutron spin echo spectroscopy

Taro Nakajima [1,2,*] Tatsuro Oda,[3] Masahiro Hino,[3] Hitoshi Endo,[4] Kazuki Ohishi,[5] Kazuhisa Kakurai,[2,5]
Akiko Kikkawa,[2] Yasujiro Taguchi,[2] Yoshinori Tokura,[2,6] and Taka-hisa Arima[2,7]

[1]*The Institute for Solid State Physics, University of Tokyo, Kashiwa, Chiba, Japan*
[2]*RIKEN Center for Emergent Matter Science (CEMS), Saitama 351-0198, Japan*
[3]*Institute for Integrated Radiation and Nuclear Science, Kyoto University, Kumatori, Osaka 590-0494, Japan*
[4]*Institute of Materials Structure Science, and Materials and Life Science Division, J-PARC Center, High Energy Accelerator Research
Organization, Tokai, Ibaraki 319-1106, Japan*
[5]*Neutron Science and Technology Center, Comprehensive Research Organization for Science and Society (CROSS), Tokai,
Ibaraki 319-1106, Japan*
[6]*Department of Applied Physics and Tokyo College, University of Tokyo, Tokyo 113-8656, Japan*
[7]*Department of Advanced Materials Science, University of Tokyo, Kashiwa 277-8561, Japan*

We performed neutron resonance spin echo measurements on MnSi to investigate how the magnetic skyrmions crystalize into a lattice on cooling in a magnetic field. We found that the skyrmions aggregate into small skyrmion-lattice (SkL) domains with orientational disorder upon the transition from the paramagnetic phase to the SkL phase. These domains are nearly static in time, and coexist with chiral spin fluctuations with a characteristic relaxation time of 10^{-9} s near the transition temperature. As the temperature is further decreased, the SkL domains merge into the long-range-ordered SkL. These observations provide a microscopic picture of the crystallization of the magnetic skyrmions.

I. INTRODUCTION

Magnetic skyrmions are nanometric vortexlike spin objects [1–3]. They can be regarded as topological defects in a ferromagnetic spin arrangement, and thus behave like particles, which have been indeed observed in previous Lorentz transmission electron microscopy studies [2,4]. Recent studies on metastable skyrmion states further evidenced the robustness of the particle nature at low temperatures; while magnetic skyrmions in a bulk chiral magnet often appear as a thermoequilibrium skyrmion-lattice (SkL) state in a narrow phase pocket just below the critical temperature T_c, they can also persist as a metastable state when being quenched to low temperatures [5–9]. This is indicative of an energy barrier for the transformation from the particlelike spin texture to other magnetic structures, and thus it is often mentioned that the skyrmions are "topologically protected" [8,10]. In contrast to the pronounced particle nature at low temperatures, it remains to be investigated how the particle nature starts showing up upon the phase transition from the paramagnetic (PM) phase to the SkL phase.

There are a number of key experiments regarding this issue. Previous high-precision specific-heat measurements on an archetypal skyrmion compound MnSi revealed a sharp peak anomaly in heat capacity at the boundary between the SkL and PM phases, indicating that the phase transition between these phases is of the first order [11]. It is also known that MnSi exhibits highly isotropic chiral spin fluctuations just above T_c in the PM phase [12–17]. Interestingly, a recent comprehensive experimental study on MnSi reported that skyrmionlike spin correlation appears in the chiral spin fluctuation state at around T_c in a magnetic field [16]. From the viewpoint of the first-order phase transition, one may expect that the skyrmions and the chiral spin fluctuations coexist near T_c, and that they have different spin dynamics from each other. Thus, it is important to investigate spatiotemporal correlation of magnetic moments in the possible phase coexistence regime, which leads to a microscopic picture of the crystallization of the magnetic skyrmions from the PM state.

In this study, we investigate the PM-to-SkL transition in MnSi by means of neutron spin echo (NSE) spectroscopy, which is suited for probing diffusive dynamics with the timescales of the order of picoseconds to submicroseconds. Actually, the chiral spin fluctuations in MnSi were studied by means of polarimetric and ferromagnetic NSE measurements [13,15,17], in which the Larmor precession of polarized neutron spin is utilized for detecting very small changes in neutron velocity upon quasielastic scattering processes. However, neither the polarimetric nor ferromagnetic NSE is suited for the SkL phase. The former is limited to zero-field measurements. Although the latter is applicable for in-field measurements, the noncollinear spin arrangement of the SkL leads to mixing of spin-flip and non-spin-flip scatterings, which substantially reduces the signal contrast [15]. In this study,

*taro.nakajima@issp.u-tokyo.ac.jp

we thus employ the neutron resonance spin echo technique. In particular, we use the modulation-of-intensity-with-zero-effort (MIEZE) method [18], in which the intermediate spin correlation function $I(Q, t) = S(Q, t)/S(Q, 0)$, where $S(Q, t)$ is the temporally Fourier-transformed dynamical structure factor, is obtained not from the final neutron spin polarization after experienced the precessions mentioned above, but from beating patterns of scattered neutron intensities (MIEZE signals) as a function of time. Since the MIEZE signals are independent of the spin state of scattered neutrons, this technique is suited for measuring magnetic scattering in magnetic field, and was in fact applied to SkL in the recent study on MnSi [16].

II. EXPERIMENTAL DETAILS

A single crystal of MnSi was grown by the Czochralski method, and was cut into a cylindrical shape with diameter and length of approximately 5 and 20 mm, respectively. By x-ray Laue diffraction measurements, we confirmed that the cylinder axis of the sample was parallel to the [110] axis of the crystal structure, which belongs to the chiral cubic space group of $P2_13$. The sample was sealed in an Al-cell with ^{4}He gas, and the Al cell was mounted on a closed-cycle ^{4}He refrigerator, so that the cylinder axis was vertical.

We performed MIEZE-type NSE measurements on the single crystal of MnSi at the VIN ROSE beamline (BL06) [19,20] in the materials and life science experimental facility (MLF) of J-PARC, which provides pulsed polychromatic neutron beams. Figure 1(a) shows the experimental setup of the MIEZE spectrometer. We introduce Cartesian coordinates xyz, as shown in Fig. 1(a), where the y and z axes are vertical and parallel to the incident neutron beam at the sample position, respectively. The x axis is defined so as to complete the right-hand set. A spin-polarized incident neutron beam was obtained by supermirror polarizers. A weak magnetic field of approximately 0.5 mT was applied in the beam path from the polarizers to a spin analyzer to maintain the spin polarization.
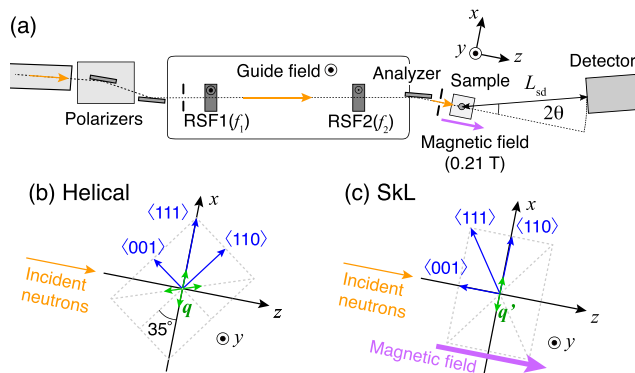
(a)

(b) Helical (c) SkL

FIG. 1. (a) Beam-line layout of the VIN ROSE (BL06) in MLF of J-PARC. (b), (c) Relationships between the orientation of the crystallographic axes and the incident neutron beam for the measurements in the (b) helical and (c) SkL phases. In (b), small (green) arrows labeled q denote directions of the magnetic modulation wave vectors (q vectors) of the helical magnetic order. In (c), small arrows labeled q' are projections of the q vectors of the SkL phase on the xz plane.

We employed a pair of resonance spin flippers [labeled RSF1 and RSF2 in Fig. 1(a)], which applied different frequencies of radio-frequency (rf) fields, specifically, $f_1 = 200$ kHz and $f_2 = 400$ kHz, respectively. Amplitudes of the rf fields were modulated in time taking into account the velocity spread of the polychromatic neutron beam, which enabled us to control probabilities of flipping the neutron spins in a wide range of the neutron wavelengths. The flipping probabilities at RSF1 and RSF2 were tuned to 50% for all the wavelengths; in other words, both RSF1 and RSF2 acted as $\frac{\pi}{2}$ flippers. After passing through RSF1 and RSF2, the wave function of the incident neutron beam was composed of four states with different energies. Finally, two of them with "down" spins were removed by a supermirror spin analyzer. As a result, the wave function of the incident neutron beam at the sample position was a superposition of the two spin-up states with different energies, which led to the intensity modulation with a frequency of $f_M (= f_2 - f_1) = 200$ kHz [18,21]. The incident neutron beam at the sample position has a size of approximately 5×5 mm^2. Only the central part of the sample (5 mm in length along the cylinder axis) was exposed to the neutron beam. The scattered neutrons were detected by a two-dimensional time-and-position-sensitive detector.

In MIEZE-type NSE experiments, the Fourier time t of the intermediate scattering function $I(Q, t)$ is given by

$$t = \left(\frac{m}{h}\right)^2 f_M L_{sd} \lambda^3, \tag{1}$$

where m and h are the neutron mass and the Planck constant, respectively. L_{sd} is a distance between the sample and the detector, which was 1.65 m in the present experiment. λ is a neutron wavelength, which is precisely determined from time of flight (TOF) of each neutron. Substituting the wavelengths range of the incident neutron beam at VIN ROSE, which spans from 3.7 to 11.3 Å, into Eq. (1), the Fourier time range is deduced to be from 0.1 to 3 ns. Note that this TOF-MIEZE method enables us to measure the $I(Q, t)$ values with different sets of Q and t simultaneously [21].

Prior to the measurements on the SkL phase, we checked the orientation of the crystal by measuring a magnetic Bragg reflection in the helical phase, in which the magnetic modulation wave vectors are (q, q, q) and its equivalents, at 5 K in zero magnetic field. We confirmed that the sample was in the orientation shown in Fig. 1(b). We then measured MIEZE signals of the Bragg reflection in the helical phase, where the Bragg scattering signals are supposed to be dominated by elastic scatterings. The contrast of the intensity modulations in the helical phase is shown in Appendix A.

For the measurements in the SkL phase, the incident neutron beam was set to be parallel to the [001] axis of the crystal, by rotating the cryostat by 35° using a goniometer, as shown in Fig. 1(c). We also applied a magnetic field of 0.21 T along the [001] axis by a magnetic circuit consisting of permanent magnets. We measured the field magnitude near the sample position by a Gauss meter, revealing that the change in magnetic field was less than 1.5% within a distance of 10 mm from the center. The orientation of the magnetic field was adjusted by measuring a magnetic Brag reflection in the SkL phase, which is known to appear on a plane perpendicular to the field. Since the detector was not large enough to cover a whole
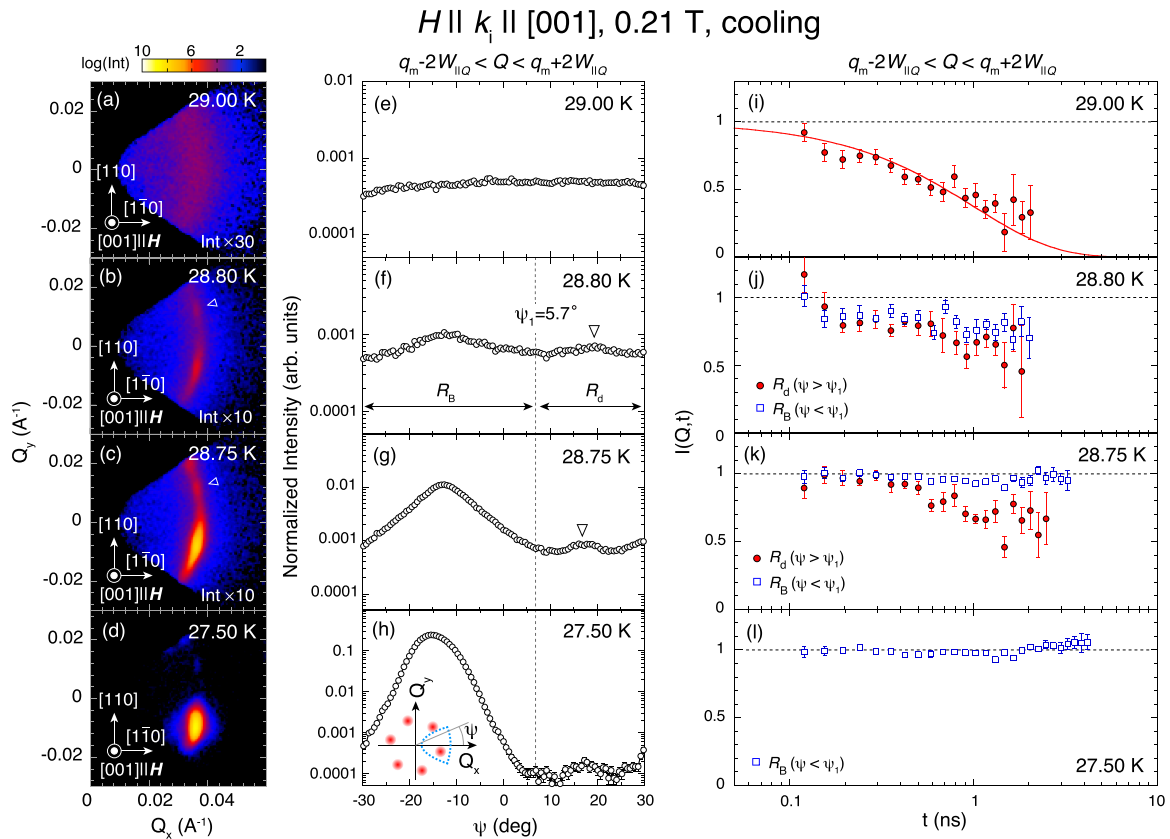
FIG. 2. (a)–(d) Intensities of scattered neutrons projected on the Q_x-Q_y plane measured at (a) 29.00, (b) 28.80, (c) 28.75, and (d) 27.50 K on cooling, where the magnetic field and incident neutron beam are parallel to the [001] ($\| Q_z$) direction. (e)–(h) ψ profiles of the annular-integrated intensities. Inset of (h) schematically shows the accessible area in the Q_x-Q_y plane and the definition of the ψ angle. Open triangles in (b), (c), (f), and (g) show the peak positions corresponding to the 30°-rotated metastable SkL domains (see the main text for details.) (i)–(l) $I(Q, t)$ profiles at each temperature. For (i), the intensities in the Q range from $q_m - 2W_{\|Q}$ to $q_m + 2W_{\|Q}$ are used to obtain the $I(Q, t)$ values. A red solid curve shows the fitted curve with the single exponential decay model. For (j) and (k), the annular-integrated area is divided into R_B ($\psi < \psi_1$) and R_d ($\psi < \psi_1$).

scattering pattern of the SkL, we focused on a small part of the reciprocal lattice space, in which one of the sixfold Bragg reflections of SkL was observed, as illustrated in the inset of Fig. 2(h). Demagnetization correction was not taken into account. However, the effective magnetic field in the sample was presumably homogeneous considering the shape of the sample and the volume exposed to the neutron beam.

$I(Q, t)$ values in the magnetic field were obtained by normalizing the contrasts of the intensity modulations to that measured at 5 K in zero field. Note that the phase of the intensity oscillation is highly sensitive to L_{sd}, which can vary depending on the scattering angle and an imperfect alignment of the detector surface. We thus developed a method for flight-path-length correction [20], and also confirmed that the resolution contrast does not depend on the positions on the detector surface.

III. RESULTS AND DISCUSSIONS

To provide an overview of the PM-to-SkL phase transition in MnSi, we show intensity maps [Figs. 2(a)–2(d)] and azimuthal angle (ψ) profiles of the radial-integrated intensities [Figs. 2(e)–2(h)] measured on cooling in a magnetic field of 0.21 T. Note that the radial integration range for the ψ profiles

is from $q_m - 2W_{\|Q}$ to $q_m + 2W_{\|Q}$, where q_m is the magnetic modulation wave number at each temperature. $W_{\|Q}$ is the half-width at half-maximum of the annular-integrated scattering profile along the radial direction at each temperature. These data show that the PM-to-SkL transition is well characterized by a change in scattering profile from the isotropic ringlike diffuse scattering [see Figs. 2(a) and 2(e)] to a sharp Bragg peak [Figs. 2(d) and 2(h)], similarly to the phase transition in zero field [13,15–17].

The $I(Q, t)$ profiles provide further insights into the spin dynamics. At 29 K, the spin correlation decays with t as shown in Fig. 2(i), indicating that the ringlike diffuse scattering indeed originates from the spin fluctuations. By fitting an exponential decay $I(Q, t) = \exp(-t/\tau)$ to the data, the characteristic time τ of the spin fluctuations is estimated to be 1.02(5) ns, which is in good agreement with the previous NSE studies on MnSi [13,15–17]. At 27.5 K, $I(Q, t)$ does not deviate from unity, as shown in Fig. 2(l), indicating that there are no spin fluctuations in the time range of $t \leqslant 3$ ns at this temperature.

We now focus on the spin fluctuations just below T_c, specifically, at 28.80 and at 28.75 K. As shown in Figs. 2(j) and 2(k), we obtain the $I(Q, t)$ profiles for the two ψ ranges of R_B ($\psi < \psi_1$) and R_d ($\psi > \psi_1$), where $\psi_1 = 5.7°$; the former
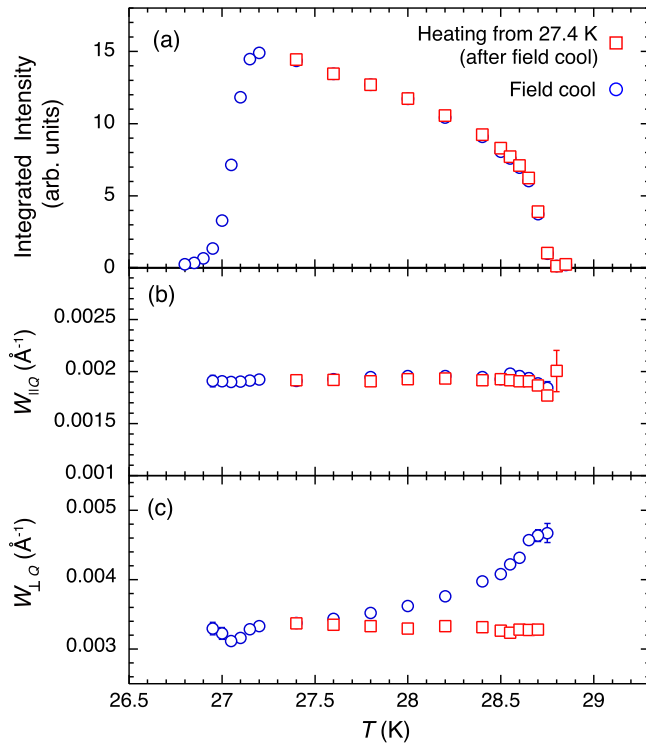
FIG. 3. Temperature variations of (a) integrated intensity, (b) half-width at half-maximum of the magnetic Bragg peak along the radial direction $W_{\parallel Q}$, and (c) that for the azimuthal direction $W_{\perp Q}$ measured in a magnetic field of 0.21 T applied parallel to the [001] direction. Note that we first obtained the azimuthal widths in radian units $W'_{\perp Q}$ by fitting a Gaussian function to the ψ profile at each temperature, and then converted them into the widths in Å^{-1} units, $W_{\perp Q}$, using a formula of $W_{\perp Q} = q_m W'_{\perp Q}$. Blue circles and red squares show data measured on cooling and heating, respectively. The heating data were obtained after the sample was cooled to 27.4 K in the magnetic field.

and latter ranges correspond to the Bragg peak and diffuse scattering, respectively. As the Bragg peak starts to grow, the $I(Q, t)$ value in R_B approaches unity. On the other hand, that in R_d still decays with t. This indicates that the magnetic moments involved in the Bragg peak are freezing, and that the remaining part is still fluctuating at these temperatures.

We have also found that the Bragg peak from the SkL has an anisotropic profile just below T_C; the width along the azimuthal direction is rather broad as compared to that along the radial direction, as shown in Figs. 2(b) and 2(c). The anisotropic broadening becomes less significant at 27.5 K [Fig. 2(d)]. We thus measured temperature variations of intensity, the radial and azimuthal widths $W_{\parallel Q}$ and $W_{\perp Q}$ of the Bragg peak in more detail without NSE option, as shown in Figs. 3(a)–3(c), respectively. $W_{\parallel Q}$ is nearly independent of temperature regardless of the direction of the temperature sweep. By contrast, $W_{\perp Q}$ exhibits a significant thermal hysteresis. As shown in Fig. 3(c), the peak broadening along the ψ direction at higher temperatures is observed only on cooling. In Fig. 4, we also show temperature dependence of integrated intensities in the regions of R_B and R_d on cooling. We found that the diffuse scattering in R_d is maximized at around 28.7 K, and that it is sharply reduced as the Bragg
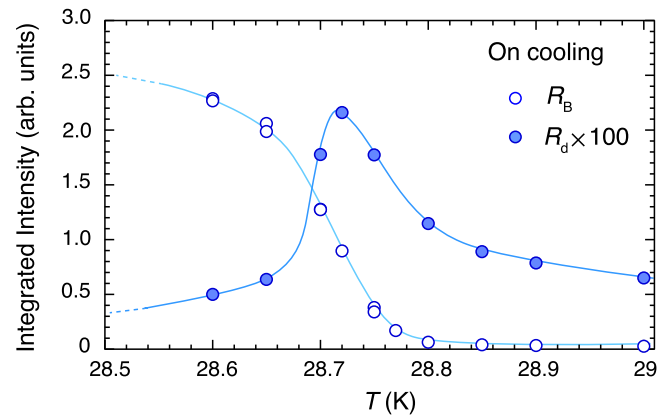

FIG. 4. Temperature dependence of the integrated intensities in the regions of R_B and R_d measured on cooling in a magnetic field of 0.21 T. The latter is multiplied by 100 for the visibility. Solid lines are guides to the eyes.

peak in R_B develops. We also note that $W_{\perp Q}$ is still relatively large after the abrupt reduction of the diffuse intensity. As the temperature is further reduced, $W_{\perp Q}$ gradually decreases as shown in Fig. 3(c). Once $W_{\perp Q}$ is reduced to the value at 27.4 K, it stays constant on subsequent heating.

These observations can be interpreted as follows. When the skyrmions appear upon cooling in a magnetic field, they start aggregating into a triangular lattice, but cannot immediately achieve a true long-range order just below T_C. Then, the system is composed of triangular SkL domains with orientational disorder, which leads to the broadening of the Bragg peak along the ψ direction. Despite the orientational disorder, the spacing between neighboring skyrmions in each domain seems to be quite regular, as inferred from the fact that $W_{\parallel Q}$ is always as small as that in the middle of the SkL phase. These small SkL domains coexist with the chiral spin fluctuations near T_C. As the temperature is decreased, the chiral spin fluctuations are rapidly reduced below T_C, and the small SkL domains gradually merge into a long-range-ordered (LRO) state. Once the LRO-SkL state is achieved, it remains stable on heating. A recent small-angle neutron scattering study has also reported broadening of Bragg reflections in the SkL phase of MnSi with varying magnetic field at a fixed temperature [22]. This suggests that the progressive aggregation of the magnetic skyrmions is also occurring upon the field-induced phase transition to the SkL phase.

To confirm this scenario, we investigate the ψ dependence of $I(Q, t)$ in more detail. In Fig. 3(a), we show the ψ profile at 28.75 K in a linear scale. A dotted line shows the ψ profile at 27.5 K normalized and shifted to the height and peak center at 28.75 K, respectively. We divide R_B into three regions as shown in Fig. 3(a), so that $R_B^{(1)}$ and $R_B^{(3)}$ mainly contain the intensities due to the peak broadening, while $R_B^{(2)}$ picks up those near the peak center. As shown in Figs. 5(b)–5(d), the $I(Q, t)$ in these three regions are close to 1.0, as distinct from the apparent decay in R_d shown in Fig. 5(e). This suggests that the origin of the peak broadening is not the critical scattering, which is known to appear in a second-order phase transition, but the existence of small domains with rotational disorder, which are nearly static in time.
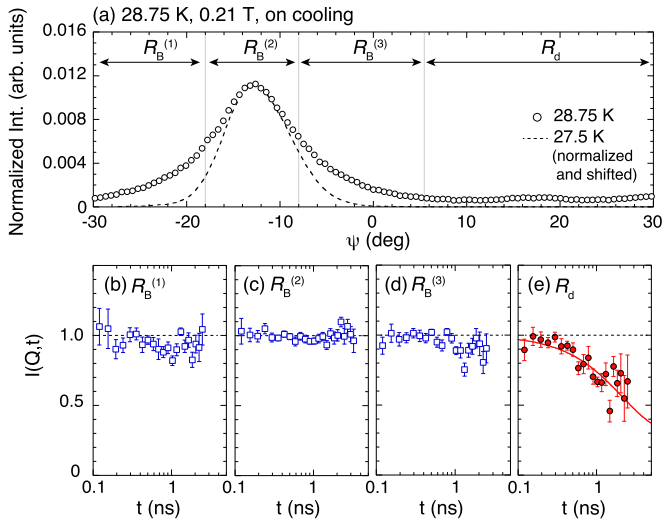
FIG. 5. (a) ψ dependence of the radial integrated intensity at 28.75 K [the same data as shown in Fig. 2(g)]. A dotted line shows the ψ profile at 27.5 K. Note that the peak height and center are normalized and shifted to those at 28.75 K. (b)–(d) $I(Q,t)$ profiles in the regions of (b) $R_B^{(1)}$, (c) $R_B^{(2)}$, (d) $R_B^{(3)}$, and (e) R_d. A red solid curve in (e) shows the fitted curve with the single exponential decay with a static component.

We also note that the ψ profiles at 28.80 and 28.75 K show a small peak at around $\psi = 18°$, which is located approximately 30° away in azimuthal direction from the main Bragg peak, as indicated by triangles in Figs. 2(f) and 2(g). This peak is also visible in the intensity maps shown in Figs. 2(b) and 2(c). The SkL reflections at an interval of 30° have been reported in a cubic chiral magnet Co-Zn-Mn alloy [6] and tetragonal polar magnet VOSe$_2$O$_5$ [23], both of which have at least one fourfold-rotational symmetry axis. Since the triangular SkL is not compatible with the fourfold symmetry, the 90° rotation should produce two SkL domains, which are energetically equivalent to each other, in these systems. In contrast, MnSi, which belongs to the space group of $P2_13$, does not have any fourfold axes. Therefore, 30°-rotated SkL domains appear only as a metastable state. The present results suggest that a small fraction of the SkL domains are stuck in the metastable orientation during the aggregation process near T_c upon cooling. As the temperature is further decreased, the intensities in R_d are significantly reduced as seen in Fig. 2(h). A very small peak at around $\psi = 18°$ seems to still remain at 27.50 K, which suggests that a tiny fraction of the SkL domains are still in the metastable orientation at this temperature. Note that it was impossible to obtain $I(Q,t)$ curve for R_d at 27.50 K because of the extremely weak intensity.

The coexistence of the 30°-rotated SkL domains was also observed in Cu$_2$OSeO$_3$ [24,25] and (Fe,Co)Si [26]; neither of their crystal structures has fourfold-rotational symmetry. In Cu$_2$OSeO$_3$, it was reported that the most stable orientation of the SkL changes with temperature and magnetic field [24]. In addition, there is a relatively large energy barrier between the SkL states with the different orientations [25]. Therefore, the coexistence of the two SkLs is ascribed to the metastability of these SkL states. Regarding (Fe,Co)Si, an application of a magnetic field parallel to the ⟨001⟩ direction induces two

SkL domains with a relative angle of 30°, one of which has significantly weaker intensities than the other [26]. This is quite similar to the present results on MnSi, implying that on the (001) plane in (Fe,Co)Si and MnSi, the two SkLs are energetically close to each other, but the degeneracy is lifted due to the absence of the fourfold-rotational symmetry.

If we assume that the 30°-rotated SkL domains are also static in time, the $I(Q,t)$ curve in R_d can be described as $a + (1 - a)\exp(-t/\tau)$; the first and second terms correspond to the static and fluctuating components, respectively. We thus estimate the integrated intensities of the small peak and the tail of the main peak at 28.75 K, as shown in Appendix B, revealing that the ratio of the possible static fraction to the total intensity in R_d is approximately 0.3. In Fig. 5(e), we show the fitted curve with $a = 0.3$, which shows a good agreement with the observed data. Although the Fourier time range is not wide enough to unambiguously determine a and τ from the $I(Q,t)$ data, the present results are roughly consistent with our interpretation. We also tried the fitting analyses of the $I(Q,t)$ curves at 28.80 and at 28.75 K, which are shown in Appendix C. The τ values at these temperatures were estimated to be in the range from 10^{-8} to 10^{-9} s, though the obtained parameters have relatively large errors. To precisely track the temperature dependence of a and τ, it is necessary to expand the accessible Fourier time range of the instrument.

Finally, we mention the recent MIEZE-type NSE measurements on MnSi in a magnetic field [16]. They measured $I(Q,t)$ around one of the six spots of the SkL reflections just above the phase boundary between the paramagnetic and SkL phases, concluding that the system exhibits skyrmionlike spin textures fluctuating with lifetimes up to 10^{-9} s just above T_c. On the other hand, the present results show that the spotlike and diffuse scattering signals correspond to different spin dynamics, indicating the phase separation of the static SkL domains and chiral spin fluctuations. We have demonstrated that ψ-resolved $I(Q,t)$ analyses with high-Q resolution are necessary to distinguish these components. We also note that the direction of a magnetic field was along [110] in Ref. [16], which is different from this study. Since the orientation of the SkL is highly sensitive to the magnetocrystalline anisotropy [27], the difference in field direction could affect the peak broadening.

IV. SUMMARY

In summary, we have studied the PM-to-SkL transition in MnSi by means of MIEZE-type NSE measurements. The present results show that the skyrmions aggregate into small SkL domains with orientational disorder when the system is cooled from the PM phase. In the vicinity of the transition temperature, we observed the coexistence of the SkL domains and chiral spin fluctuations. The ψ dependence of the $I(Q,t)$ profile has revealed that the SkL domains are nearly static in time while the remaining part exhibits fluctuations with the timescale of 10^{-9} s. We note that correlation between dynamical heterogeneity and medium-range crystalline orders has been studied in numerical simulations of two-dimensional colloidal liquid [28], which may have similarity with magnetic skyrmion systems. The aggregation of magnetic skyrmions has also been experimentally observed in a recent Lorentz transmission electron microscopy study of a thin plate of FeGe
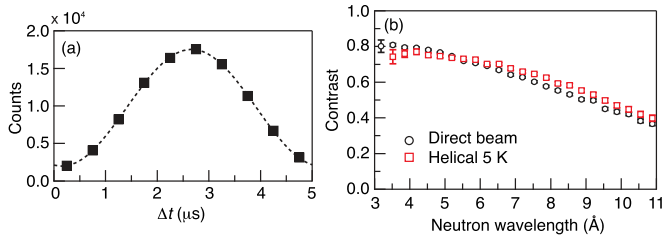
FIG. 6. (a) A typical intensity histogram as a function of Δt in a time bin corresponding to $\lambda = 4.2$ Å. (b) Contrasts of the MIEZE signal for the incident neutron beam (circles) and the scattered beam in the helical phase at 5 K in zero field (squares).

at low temperatures [29]. This study suggests that a similar aggregation process also takes place in a bulk sample, and provides a microscopic picture of the first-order transition from the PM phase to the SkL phase.

APPENDIX A: CONTRAST OF THE MIEZE SIGNALS OF THE INCIDENT NEUTRON BEAM AND THE BRAGG REFLECTION IN THE HELICAL PHASE

As mentioned in Sec. II, the neutron intensities oscillated in time with the frequency of $f_M = 200$ kHz in the present

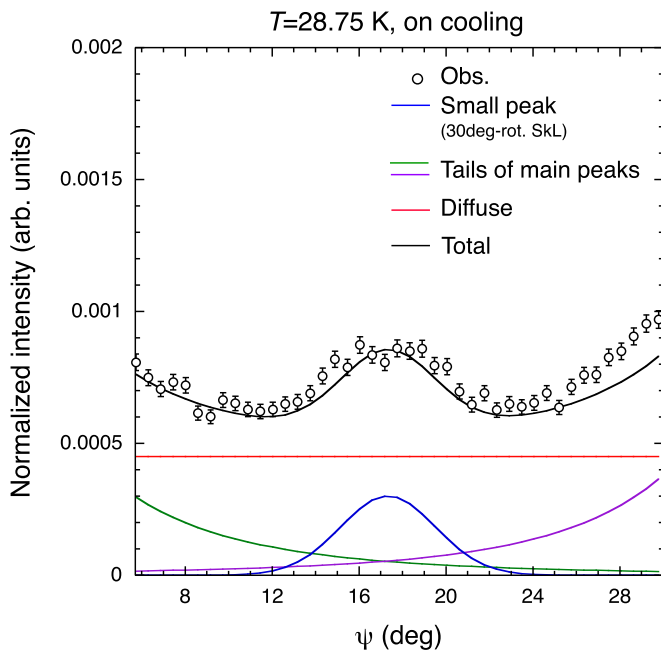MIEZE-type NSE measurements. We recorded the intensity oscillations at the detector as functions of time of flight, t_{TOF}, by which we can deduce the wavelengths of each neutron. Then, we divided the observed data into time bins with a width of 2 ms, in each of which we made a histogram of the neutron counts as a function of a reduced time Δt, which is defined as follows: $\Delta t = t_{TOF} - n/f_M$ and $0 < \Delta t < 1/f_M$ (n is an integer). After subtracting background signals, which were measured at 60 K in the same manner, we fitted a function $B + A \sin(2\pi f_M \Delta t + \delta)$ to the intensity histograms of each time bin [see Fig. 6(a) for a typical intensity profile in a time bin corresponding to $\lambda = 4.2$ Å], and obtained A and B as functions of neutron wavelength. The contrast of the intensity oscillation is defined as $C = A/B$. In Fig. 6(b), we show the contrast of the MIEZE signal of the incident beam as a function of wavelength and that of the scattered beam in the helical phase at 5 K in zero magnetic field. There was little difference between these contrasts. To obtain $I(Q, t)$ in the main text, the measured contrasts were divided by the contrast of the helical state in the same beam collimation.

APPENDIX B: INTENSITY FRACTION OF THE SMALL PEAK DUE TO THE METASTABLE SkL DOMAINS

At 28.75 and 28.80 K, we observe a small peak at around $\psi = 18°$, which corresponds to $30°$-rotated metastable SkL domains. We have estimated the integrated intensities of the

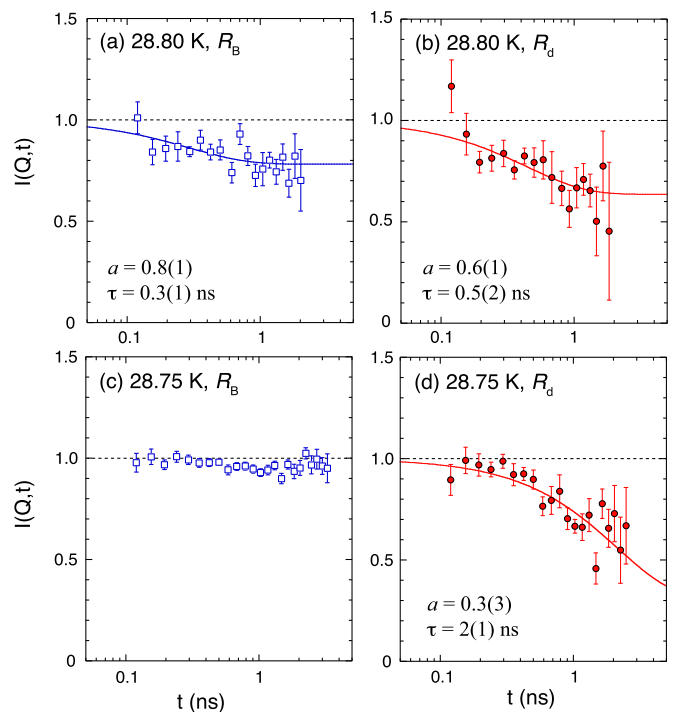FIG. 7. The result of the fitting analysis to extract possible static components from the ψ profile at 28.75 K after field cooling in a magnetic field of 0.21 T.

FIG. 8. $I(Q, t)$ profiles of (a) R_B and (b) R_d at 28.80 K and those of (c) R_B and (d) R_d at 28.75 K measured after field cooling in a magnetic field of 0.21 T. For (a), (b), and (d), we performed fitting analyses using the single exponential decay model with a static fraction $a + (1 - a)\exp(-t/\tau)$. Solid lines are the results of the fitting analyses. The parameters and their errors are shown in each panel.

small peak, tails of the main Bragg peaks, and isotropic diffuse scattering at 28.75 K, as shown in Fig. 7. The intensity ratio of the possible static components (the small peak and tails of the Bragg peaks) to the total intensity is estimated to be 0.3. The $I(Q, t)$ curve for R_d at this temperature can be reproduced by a function $a + (1 - a) \exp(-t/\tau)$, where a is fixed at 0.3, as described in the main text.

APPENDIX C: FITTING ANALYSIS OF THE $I(Q, t)$ CURVES NEAR T_C

We fitted the single exponential decay model with a static component, namely, $a + (1 - a) \exp(-t/\tau)$, to the $I(Q, t)$ profiles at 28.75 and 28.80 K. Note that no temporal decay was observed in the region R_B at 28.75 K. We thus excluded it from the fitting analysis. The parameters obtained by the fitting analysis are shown in each panel in Fig. 8. To unambiguously determine the static fraction a from the fitting analysis, it is necessary to measure longer Fourier time ranges where the $I(Q, t)$ value becomes constant. However, the Fourier time range in this study was not enough to reach that region, and thus the parameters have relatively large errors. In this analysis, both a and τ were refined as free parameters, and the value of a for R_d at 28.75 K was determined to be 0.3 ± 0.3. Although the error is quite large, this is consistent with the static fraction estimated from the ψ profile as discussed in Appendix B.

[1] S. Mühlbauer, B. Binz, F. Jonietz, C. Pfleiderer, A. Rosch, A. Neubauer, R. Georgii, and P. Böni, Skyrmion lattice in a chiral magnet, Science **323**, 915 (2009).

[2] X. Z. Yu, Y. Onose, N. Kanazawa, J. H. Park, J. H. Han, Y. Matsui, N. Nagaosa, and Y. Tokura, Real-space observation of a two-dimensional skyrmion crystal, Nature (London) **465**, 901 (2010).

[3] N. Nagaosa and Y. Tokura, Topological properties and dynamics of magnetic skyrmions, Nat. Nanotechnol. **8**, 899 (2013).

[4] H. S. Park, X. Yu, S. Aizawa, T. Tanigaki, T. Akashi, Y. Takahashi, T. Matsuda, N. Kanazawa, Y. Onose, D. Shindo, A. Tonomura, and Y. Tokura, Observation of the magnetic flux and three-dimensional structure of skyrmion lattices by electron holography, Nat. Nanotechnol. **9**, 337 (2014).

[5] H. Oike, A. Kikkawa, N. Kanazawa, Y. Taguchi, M. Kawasaki, Y. Tokura, and F. Kagawa, Interplay between topological and thermodynamic stability in a metastable magnetic skyrmion lattice, Nat. Phys. **12**, 62 (2016).

[6] K. Karube, J. S. White, N. Reynolds, J. L. Gavilano, H. Oike, A. Kikkawa, F. Kagawa, Y. Tokunaga, H. M. Rønnow, Y. Tokura, and Y. Taguchi, Robust metastable skyrmions and their triangular-square lattice structural transition in a high-temperature chiral magnet, Nat. Mater. **15**, 1237 (2016).

[7] T. Nakajima, H. Oike, A. Kikkawa, E. P. Gilbert, N. Booth, K. Kakurai, Y. Taguchi, Y. Tokura, F. Kagawa, and T.-h. Arima, Skyrmion lattice structural transition in MnSi, Sci. Adv. **3**, e1602562 (2017).

[8] J. Wild, T. N. G. Meier, S. Pöllath, M. Kronseder, A. Bauer, A. Chacon, M. Halder, M. Schowalter, A. Rosenauer, J. Zweck, J. Müller, A. Rosch, C. Pfleiderer, and C. H. Back, Entropy-limited topological protection of skyrmions, Sci. Adv. **3**, e1701704 (2017).

[9] L. J. Bannenberg, K. Kakurai, F. Qian, E. Leliévre-Berna, C. D. Dewhurst, Y. Onose, Y. Endoh, Y. Tokura, and C. Pappas, Extended skyrmion lattice scattering and long-time memory in the chiral magnet $Fe_{1-x}Co_xSi$, Phys. Rev. B **94**, 104406 (2016).

[10] P. Milde, D. Köhler, J. Seidel, L. M. Eng, A. Bauer, A. Chacon, J. Kindervater, S. Mühlbauer, C. Pfleiderer, S. Buhrandt, C. Schütte, and A. Rosch, Unwinding of a skyrmion lattice by magnetic monopoles, Science **340**, 1076 (2013).

[11] A. Bauer, M. Garst, and C. Pfleiderer, Specific Heat of the Skyrmion Lattice Phase and Field-Induced Tricritical Point in MnSi, Phys. Rev. Lett. **110**, 177207 (2013).

[12] S. V. Grigoriev, S. V. Maleyev, A. I. Okorokov, Yu. O. Chetverikov, R. Georgii, P. Böni, D. Lamago, H. Eckerlebe, and K. Pranzas, Critical fluctuations in MnSi near T_C: A polarized neutron scattering study, Phys. Rev. B **72**, 134420 (2005).

[13] C. Pappas, E. Lelièvre-Berna, P. Falus, P. M. Bentley, E. Moskvin, S. Grigoriev, P. Fouquet, and B. Farago, Chiral Paramagnetic Skyrmion-like Phase in MnSi, Phys. Rev. Lett. **102**, 197202 (2009).

[14] M. Janoschek, M. Garst, A. Bauer, P. Krautscheid, R. Georgii, P. Böni, and C. Pfleiderer, Fluctuation-induced first-order phase transition in Dzyaloshinskii-Moriya helimagnets, Phys. Rev. B **87**, 134407 (2013).

[15] C. Pappas, L. J. Bannenberg, E. Lelièvre-Berna, F. Qian, C. D. Dewhurst, R. M. Dalgliesh, D. L. Schlagel, T. A. Lograsso, and P. Falus, Magnetic Fluctuations, Precursor Phenomena, and Phase Transition in MnSi under a Magnetic Field, Phys. Rev. Lett. **119**, 047203 (2017).

[16] J. Kindervater, I. Stasinopoulos, A. Bauer, F. X. Haslbeck, F. Rucker, A. Chacon, S. Mühlbauer, C. Franz, M. Garst, D. Grundler, and C. Pfleiderer, Weak Crystallization of Fluctuating Skyrmion Textures in MnSi, Phys. Rev. X **9**, 041059 (2019).

[17] S. V. Grigoriev, S. V. Maleyev, E. V. Moskvin, V. A. Dyadkin, P. Fouquet, and H. Eckerlebe, Crossover behavior of critical helix fluctuations in MnSi, Phys. Rev. B **81**, 144413 (2010).

[18] R. Gähler, R. Golub, and T. Keller, Neutron resonance spin echo-a new tool for high resolution spectroscopy, Phys. B (Amsterdam) **180-181**, 899 (1992).

[19] M. Hino, T. Oda, N. L. Yamada, H. Endo, H. Seto, M. Kitaguchi, M. Harada, and Y. Kawabata, Supermirror neutron guide system for neutron resonance spin echo spectrometers at a pulsed neutron source, J. Nucl. Sci. Technol. **54**, 1223 (2017).

[20] T. Oda, M. Hino, H. Endo, H. Seto, and Y. Kawabata, Phys. Rev. Appl. **14**, 054032 (2020).

[21] T. Oda, M. Hino, M. Kitaguchi, P. Geltenbort, and Y. Kawabata, Pulsed neutron time-dependent intensity modulation for quasi-elastic neutron scattering spectroscopy, Rev. Sci. Instrum. **87**, 105124 (2016).

[22] A. W. D. Leishman, R. M. Menezes, G. Longbons, E. D. Bauer, M. Janoschek, D. Honecker, L. DeBeer-Schmitt, J. S. White, A. Sokolova, M. V. Milošević, and M. R. Eskildsen, Topological energy barrier for skyrmion lattice formation in MnSi, Phys. Rev. B **102**, 104416 (2020).

[23] T. Kurumaji, T. Nakajima, V. Ukleev, A. Feoktystov, T.-h. Arima, K. Kakurai, and Y. Tokura, Néel-Type Skyrmion Lattice in the Tetragonal Polar Magnet $VOSe_2O_5$, Phys. Rev. Lett. **119**, 237201 (2017).

[24] S. Seki, J.-H. Kim, D. S. Inosov, R. Georgii, B. Keimer, S. Ishiwata, and Y. Tokura, Formation and rotation of skyrmion crystal in the chiral-lattice insulator Cu_2OSeO_3, Phys. Rev. B **85**, 220406(R) (2012).

[25] K. Makino, J. D. Reim, D. Higashi, D. Okuyama, T. J. Sato, Y. Nambu, E. P. Gilbert, N. Booth, S. Seki, and Y. Tokura, Thermal stability and irreversibility of skyrmion-lattice phases in Cu_2OSeO_3, Phys. Rev. B **95**, 134412 (2017).

[26] W. Münzer, A. Neubauer, T. Adams, S. Mühlbauer, C. Franz, F. Jonietz, R. Georgii, P. Böni, B. Pedersen, M. Schmidt, A. Rosch, and C. Pfleiderer, Skyrmion lattice in the doped semiconductor $Fe_{1-x}Co_xSi$, Phys. Rev. B **81**, 041203(R) (2010).

[27] T. Adams, M. Garst, A. Bauer, R. Georgii, and C. Pfleiderer, Response of the Skyrmion Lattice in MnSi to Cubic Magnetocrystalline Anisotropies, Phys. Rev. Lett. **121**, 187205 (2018).

[28] T. Kawasaki, T. Araki, and H. Tanaka, Correlation between Dynamic Heterogeneity and Medium-Range Order in Two-Dimensional Glass-Forming Liquids, Phys. Rev. Lett. **99**, 215701 (2007).

[29] X. Yu, D. Morikawa, T. Yokouchi, K. Shibata, N. Kanazawa, F. Kagawa, T.-h. Arima, and Y. Tokura, Aggregation and collapse dynamics of skyrmions in a non-equilibrium state, Nat. Phys. **14**, 832 (2018).